Self-nested large-eddy simulations in PALM Model System v21.10 for offshore wind prediction under different atmospheric stability conditions

Maria Krutova[1], Mostafa Bakhoday-Paskyabi[1], Joachim Reuder[1], and Finn Gunnar Nielsen[1]

[1]Geophysical institute and Bergen Offshore Wind Centre, University of Bergen, Allégaten 70, 5007 Bergen, Norway

Correspondence: Maria Krutova (maria.krutova@uib.no), Mostafa Bakhoday-Paskyabi
(mostafa.bakhoday-paskyabi@uib.no)

Abstract.

Large-eddy simulation (LES) resolves large-scale turbulence directly and parametrizes small-scale turbulence. Resolving the micro-scale turbulence, e.g., in the wind turbine wakes, requires both a sufficiently small grid spacing and a domain large enough to develop the turbulent flow. Refining the grid locally via a nesting interface effectively decreases the required
5   computational time compared to the global grid refinement. However, interpolating the flow between the nested grid boundaries introduces another source of uncertainty. Previous studies reviewed the nesting effects for a buoyancy-driven flow and observed a secondary circulation in the two-way nested area. Using nesting interface with a shear-driven flow in the wind field simulation, therefore, requires additional verification. We use PALM model system to simulate the boundary layer in a cascading self-nested domain under neutral, convective, and stable conditions, and verify the results based on the wind speed measurements
10   taken at the FINO1 platform in the North Sea. We show that the feedback between the parent and child domain in a two-way nested simulation of a non-neutral boundary layer alters the circulation in the refined domain, despite the spectral characteristics following the reference measurements. Unlike the pure buoyancy-driven flow, the non-neutral shear-driven flow slows down in the two-way nested area and accelerates after exiting the child domain. We also briefly review the nesting effect on the velocity profiles and turbulence anisotropy.

1   Introduction

Large-eddy simulation allows performing a detailed process study for areas and situations where we lack appropriate the field measurements. For this reason, LES are widely used for high-fidelity simulations of the wind flows in the wind energy applications. When considering the turbulent flow, the grid resolution should be sufficiently high, so that the relevant turbulence scales are resolved (Wurps et al., 2020). Increased grid resolution comes at the cost of gradually increased computational time.
20   The overall computational time can be reduced by refining the grid locally through the nesting interface. While improving the grid resolution, the nesting may introduce new uncertainties in the simulation. Such nesting effects are documented for the buoyancy-driven flows with the strongest influence observed for the two-way nesting (Moeng et al., 2007; Hellsten et al., 2021). The buoyancy-driven flow develops a secondary circulation and decreased velocity inside the nested area – the effect

Table 1. Aggregated statistics of 1-hour sonic anemometer time series.

Stability	$\overline{U}_{119}$, ms^{-1}	TI_{119}, %	L, m	ζ	ψ	1-hour period start
NBL	12.41	6.6	2753	0.043	0	April 18, 2016 04:30
CBL	12.58	6.1	-451	-0.263	0.528	February 22, 2016 19:00
SBL	12.14	3.2	158	0.753	-3.540	June 2, 2016 16:30

becomes prominent for the data averaged over several hours. However, buoyancy-driven flows are characterized by near-zero

25 wind speed, while the wind energy research primarily deals with the wind speeds of $5 - 25\,\mathrm{ms}^{-1}$. Therefore, shear-driven simulations with the nesting interface require additional verification.

We use Fortran-based LES code PALM 21.10 (Maronga et al., 2020) to simulate the flow at the speed of $12.5\,\mathrm{ms}^{-1}$ at the hub height of $119\,\mathrm{m}$ for three stability conditions: true neutral (NBL), convective (CBL), and stable (SBL) boundary layers. The initial velocity and turbulence intensity profiles are defined to match 1-hour averages of the sonic anemometer time series

30 as processed by Nybø et al. (2019). The domain is simulated for one-way and two-way nesting modes, and without nested domains. The resulting turbulence statistics are then compared between the model results and measurements to evaluate the model performance.

2 Data

The reference measurements contain wind speed directional components u, v and w recorded with sonic anemometers during

35 the Offshore Boundary-Layer Experiment at FINO1 (OBLEX-F1) campaign in $2015-2016$ in the North Sea. The meteorological mast is installed on the FINO1 platform located in the North Sea at 54° 00′ 53.5″N, 6° 35′ 15.5″E, 45 km to the north of the German island of Borkum.

The sonic anemometers were installed at the meteorological mast at 40, 60 and 80 m. The measurements were processed by Nybø et al. (2019) and organized into one-hour time series of 1 Hz frequency. Each series corresponds to different pairs of

40 stability condition and mean wind speed at the hub height of $119\,\mathrm{m}$. Due to the computational time restrictions, we simulate only those series where the horizontal wind speed reaches approximately $\overline{U}_{119} = 12.5\,\mathrm{ms}^{-1}$ at the hub height (Table 1).

The wind speed and the turbulence intensity at the hub height should be estimated from the measurement data. Since the measurements are originally available only for three levels, the mean wind speed profile was approximated by Nybø et al. (2020) by fitting the logarithmic law

$$45 \quad \overline{u}(z) = u_{ref} \left[\frac{\ln\left(\frac{z}{z_0} - \psi\right)}{\ln\left(\frac{z_{ref}}{z_0} - \psi\right)} \right] \tag{1}$$

where the reference wind speed u_{ref} is taken for the reference height $z_{ref} = 80\,\mathrm{m}$, and the stability correction function ψ is defined as in (Stull, 1988)

$$\psi = \begin{cases} 0 & -\,\text{NBL}, \\ -2\ln\dfrac{1+x}{2} - \ln\dfrac{1+x^2}{2} + 2\arctan x - \dfrac{\pi}{2} & -\,\text{CBL}, \\ 4.7\zeta & -\,\text{SBL}, \end{cases} \qquad (2)$$

where $x = (1 - 15\zeta)^{1/4}$. The stability parameter ζ is derived from the height above the surface z and Obukhov length L as

50 $$\zeta = \frac{z}{L} \qquad (3)$$

The roughness length z_0 in Eq. (1) is therefore the fitting parameter to be found. However, the fitting result is applicable only to the mean wind speed profile. If the instantaneous measurements are extrapolated with the found roughness length and Eq. (1) to get the time series at the hub height, the variance there is strongly overestimated. The resulting turbulence intensity TI_{119} is higher than in the underlying levels. To overcome this complication, Nybø et al. (2020) calculated the variance at 80 m and

55 assumed it to be constant for all levels in order to derive the turbulence intensity profile. Since the other methods of estimating the roughness length and extrapolating the wind speed profile (Golbazi and Archer, 2019) did not perform consistently on the short 1-hour time series, we preserve Nybø et al. (2020) approach of the constant variance for all levels.

3 Methodology

3.1 PALM LES model

60 We perform a free-flow large-eddy simulation (LES) using the Fortran code PALM developed at Universität Hanover (Maronga et al., 2020). PALM utilizes a staggered Arakawa C-grid: the velocity components are defined at the grid cell edges and are shifted by a half grid spacing; the scalar variables are defined at the center of a grid cell. The subgrid-scale fluxes are resolved via the Deardorff 1.5-order closure model.

By default, PALM solves prognostic equations for the velocity components u, v, w, and potential temperature θ. If the

65 stability condition is set to the true neutral, the temperature is considered constant and the corresponding equation is not solved.

A nested simulation in PALM consists of at least one child domain inside a parent domain. Each child domain can simultaneously be a parent domain for another child domain, thus forming a cascading self-nested structure. The top-level parent domain is further referred as the root domain to make a distinction from inner parent domains. Overall, PALM supports simulation of

70 one root domain and up to 63 child domains.

The nesting algorithm is constructed in a way to optimize computational time for multiple child domains (Hellsten et al., 2021). The nested domains communicate via interpolation which is performed just before the pressure-correction step, so that the time-consuming pressure solver is run only once per the time step. The solution at the nested boundaries of a parent domain
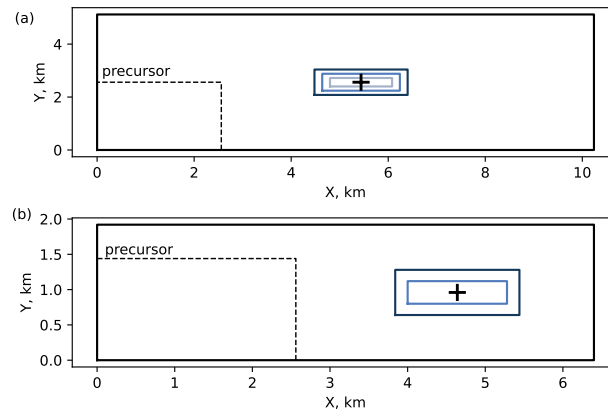
Figure 1. Nested domain schematic. (a) NBL and CBL domains, (b) SBL domains.

– velocity components and scalar quantities, e.g., temperature and humidity – is linearly interpolated into the refined grid as
boundary conditions. The prognostic equations are solved for the child domain and, in the case of the cascading nesting, the
procedure is repeated until the solution is found for all nested domains at the current step. In the one-way nesting case, the
simulation proceeds to the pressure-correction step, so the solution in the parent domains remains unaffected by the solutions
in the child domains. In the two-way nesting case, each child domain interpolates its solution back to the respective parent
domain before the pressure-correction step. Therefore, the two-way nested solution remains similar in the nested area, while
the one-way nested solution may eventually diverge for parent and child domains.

3.2 Precursor and main LES run parameters

One of the ways PALM can simulate a turbulent flow is a precursor-main run scheme, which does not require require complex
input data and effectively reduces the domain size required for the turbulence development and (Witha et al., 2014). First,
a small precursor domain is simulated with the cyclic boundaries until the flow reaches steady state. The resulting profiles
are then copied over the main domain to set up the initial non-cyclic flow with the developed turbulence. The width of the
precursor domain is usually smaller than for the main run and y-shift procedure is performed on the cyclic boundaries to avoid
non-physical regularity of the flow (Munters et al., 2016). Using the precursor-main run scheme also ensures that the idealized
input flow remains the same within the stability case regarded.

The grid characteristics of the root and innermost child domain in the PALM simulation were selected to closely match
the SOWFA simulation in Nybø et al. (2020). The ratio between parent and child domain grid spacing thus would reach 8
(from 10 m to 1.25 m for NBL and CBL cases) or 4 (from 5 m to 1.25 m for SBL case). As shown by Hellsten et al. (2021),
the discrepancy with a fine-grid simulation in PALM increases if the grid spacing ratio is 4 or higher. Therefore, we add
intermediate child domains and reduce the grid spacing by a factor of 2 until the desired refinement is reached. Hence, NBL
and CBL simulations contain three child domains, while the SBL simulation has two (Table 2, 3, Fig. 1).

Table 2. Grid parameters for NBL and CBL nested domains (Fig. 1a).

Domain	N_x	N_y	N_z	Δ_x, m	Bottom-left corner x, m	y, m
Precursor	256	256	160	10	-	-
Precursor	512	512	256	5	-	-
Root	1024	512	160	10	-	-
Child #1	384	192	128	5	4480	2080
Child #2	640	256	192	2.5	4640	2240
Child #3	1024	256	256	1.25	4800	2400

Table 3. Grid parameters for SBL nested domains (Fig. 1b).

Domain	N_x	N_y	N_z	Δ_x, m	Bottom-left corner x, m	y, m
Precursor	512	288	160	5	-	-
Root	1280	384	160	5	-	-
Child #1	640	256	192	2.5	3840	640
Child #2	1024	256	256	1.25	4000	800

We perform one-way and two-way nested simulations. To evaluate the nesting effect, we also simulate domains without
nested grids using the same input parameters. Due to the high computational time and memory requirements, we only simulate
non-nested domains for the grid spacing of $\Delta_x = 10\,\mathrm{m}$ and $5\,\mathrm{m}$.

The input parameters are selected so that the LES profiles of the mean wind speed and turbulence intensity profiles follow
the values estimated from the measurements, particularly, at the hub height. The Coriolis force is switched off; hence the
required wind speed and turbulence intensity profiles in the precursor run are obtained by a combination of the parameters:
the geostrophic mean wind $\overline{U}$, the pressure gradient forcing dp/dx, and the roughness length z_0. The NBL case is run as the
true neutral flow with no heat flux. The CBL case is defined via the positive heat flux $\overline{w'\theta'}$ in addition to the aforementioned
parameters. The SBL case uses surface cooling over time dT_s/dt instead of the heat flux (Wurps et al., 2020). The surface
temperature T_s varies to match the conditions observed during the reference meteorological measurements at FINO1. The
model setup parameters are listed in Tables $2-4$.

We run main simulations for one hour with the fixed time step of $\Delta t = 0.05\,\mathrm{s}$. Then, we probe the time series of each wind
speed component at the center of the innermost child domain and corresponding points of the parent domains (Fig. 1). The
time series are further used to compare turbulence statistics to the measurements.

Table 4. Inflow parameters of the precursor runs.

	U, ms^{-1}	dp/dx, Pa m^{-1}	z_0, m	T_s, K	$\overline{w'\theta'}$, K ms^{-1}	dT_s/dt, Ks^{-1}
NBL	13.8	-2×10^{-4}	1.2×10^{-3}	280.0	0	–
CBL (flux)	11.5	-1×10^{-4}	5×10^{-4}	281.3	0.015	–
SBL (surface)	13.0	-5×10^{-4}	8×10^{-4}	289.5	–	-0.2

3.3 Turbulence characteristics

110 We evaluate the model performance based on turbulence characteristics: power spectrum, coherence, co-coherence and phase. The coherence represents the correlation between time series $a(t)$ and $b(t)$ at two points separated by a certain distance δ and is calculated as follows

$$C_{ab} = \frac{S_{ab}}{\sqrt{S_{aa}S_{bb}}} \tag{4}$$

where S_{aa} and S_{bb} are the spectral densities at points a and b, while S_{ab} is the cross-spectrum between the same points.

115 The co-coherence represents the real part of the coherence

$$C_{ab} = \mathrm{Re}\, \frac{S_{ab}}{\sqrt{S_{aa}S_{bb}}} \tag{5}$$

The phase ϕ_{ab} shows the level of synchrony between points a and b

$$\phi_{ab} = \arctan\frac{\mathrm{Re}\, C_{ab}}{\mathrm{Im}\, C_{ab}} \tag{6}$$

Since the measurement time series are available only for three levels: 40, 60 and 80 m, the spectra are calculated and com-
120 pared at $h = 80$ m for all three components. The co-coherence is calculated for two vertical separations of $\delta = 20$ m (between levels 60 and 80 m) and $\delta = 40$ m (between levels 40 and 80 m). The sampling frequency for the LES time series matches the output frequency $f_s^{LES} = 1/0.05\,\mathrm{s} = 20\,\mathrm{Hz}$ and the segment length is chosen as 60 s. The sampling frequency for the measurement time series is lower $f_s^{mast} = 1/0.1\,\mathrm{s} = 10\,\mathrm{Hz}$, although the segment length is left the same.

3.4 Flow characteristics for load analysis

125 We review additional characteristics of the flow which are relevant for the turbine performance analysis: power law coefficient and turbulence anisotropy.

The power law is commonly applied to assess the wind resources at the hub height from the near-surface wind speed measurements.

$$U(z) = \overline{U}_{10}\left(\frac{z}{10}\right)^{\alpha} \tag{7}$$

130 where $\overline{U}_{10}$ is the wind speed at $z = 10$ m and α is the power law coefficient. The power law exponent is sensitive to the atmospheric conditions and is usually approximated with the constants, e.g., $\alpha = 1/7$ for neutral onshore sites. Often, the

Table 5. CPU time in seconds used per second of simulated time.

Stability	non-nested	one-way	two-way
NBL ($\Delta_x = 10\,\mathrm{m}$)	5.1	18.4	20.9
NBL ($\Delta_x = 5\,\mathrm{m}$)	31.7	-	-
CBL	7.9	28.8	30.8
SBL	2.8	17.4	19.7

approximations do not reflect seasonal and diurnal variations in the wind profiles (Bratton and Womeldorf, 2011; Jung and Schindler, 2021). Hence, simulating long time series with the LES gives a possibility to study wind profiles in detail.

135 The anisotropic turbulence naturally develops in a simulation with anisotropic grid resolution (Haering et al., 2019), but may also occur in the isotropic grids, such as used in this study. The anisotropic turbulence affects wind turbine loads, particularly, fatigue loads, therefore it is important to evaluate its strength in the simulation (Dimitrov et al., 2017). We estimate turbulence anisotropy by comparing spectra of the velocity components for the reduced frequency $f_r > 1$. Since the LES spectra does not resolve the inertial subrange fully, we take the bin-averaged spectra and select the bin at the beginning of the range $fz/U_z > 1$ for $z = 80\,\mathrm{m}$. We compute ratios S_{vv}/S_{uu} and S_{ww}/S_{uu} for all regarded cases. The closer both ratios are to the theoretical

140 value of $4/3 = 1.333$, the more isotropic is the simulated turbulence (Smedman et al., 2003).

4 Results

4.1 Nesting effects

All LESs are run at 1024 cores for each case; the required simulation times for each scenario are summarized in Table 5. Since the domains vary in size and number of grid points, we compare not the total CPU time, but CPU time per second of

145 the simulated time. The non-nested coarse domain ($\Delta_x = 10\,\mathrm{m}$) is not computationally demanding regardless of the stability case. However, the required CPU time gradually increases if the grid spacing is reduced globally for the whole domain. As could be seen for the NBL case, the CPU time per second of the simulated time increases from $5.1\,\mathrm{s}$ for $\Delta_x = 10\,\mathrm{m}$ to $31.7\,\mathrm{s}$ for $\Delta_x = 5\,\mathrm{m}$, respectively. Refining the grid locally with the child domains increases the CPU time compared to the coarse reference non-nested grid ($\Delta_x = 10\,\mathrm{m}$). Still, the nested simulation finishes faster than the globally refined non-nested

150 simulation ($\Delta_x = 5\,\mathrm{m}$), while allowing better local grid refinement up to $\Delta_x = 1.25\,\mathrm{m}$.

Both the NBL and CBL simulations have exactly the same domain structure and grid spacing (Table 2). However, the CBL simulations require more CPU time compared to the respective NBL (true neutral) simulations due to solving the temperature equation. The SBL simulations use CPU time comparable to the NBL simulation due to having one child domain less and the smaller root domain size – and thus a lower overall number of the grid points (Table 3).
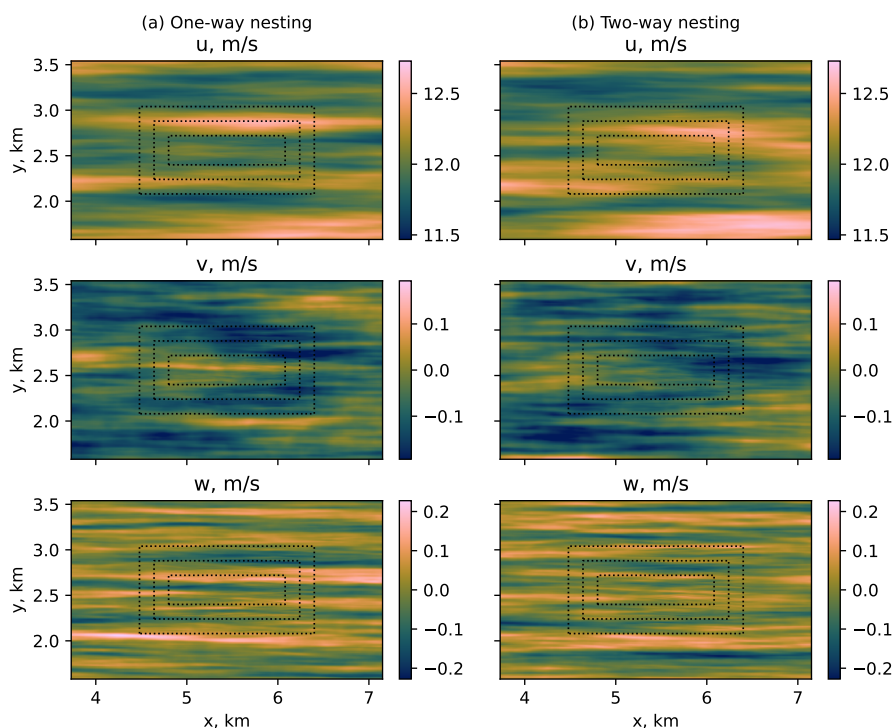
Figure 2. NBL, flow at the hub-height of 119 m for different wind speed components, (a) one-way nesting, (b) two-way nesting.

155   The two-way nested simulation required additional $\sim 2\,\mathrm{s}$ of the CPU time per simulated time step to interpolate the child domain solution back to the parent domain. This resulted in about 10% increase of the CPU time compared to the one-way nesting.

Depending on the domain configuration, LES produces different results in the area of the refined grid. In the absence of the surface heat fluxes, i.e., in the true neutral case, the one-way and the two-way nested simulations behave similarly with the
160   respect to grid spacing and feedback between domains. When the heat fluxes are introduced for the CBL and SBL simulations, the two-way simulation results in the decreased flow speed in the child domains.

Since the child domains interpolate their solution back to the parent domain, the area of reduced flow speed spreads up to the root domain. While the effect is less prominent for the instantaneous fields, it becomes clearly apparent in the 10-minute averaged flow (Fig. 3). The induction of downward vertical wind in nested simulations with PALM were already described
165   by Hellsten et al. (2021) for the 5-hour averaged buoyancy-driven flow. Hellsten et al. (2021) argued that the effect of the secondary circulation described by Moeng et al. (2007) was caused solely by the insufficient domain size and explained it with the different grid spacing and subsequent divergence of the vertical heat flux in the parent and domains. The researchers hypothesized that the secondary circulation was an inevitable side effect of the two-way nesting solution due to the better resolution of the turbulence mixing in child domains. In the case of the shear-driven flow, we observe that the slowing effect
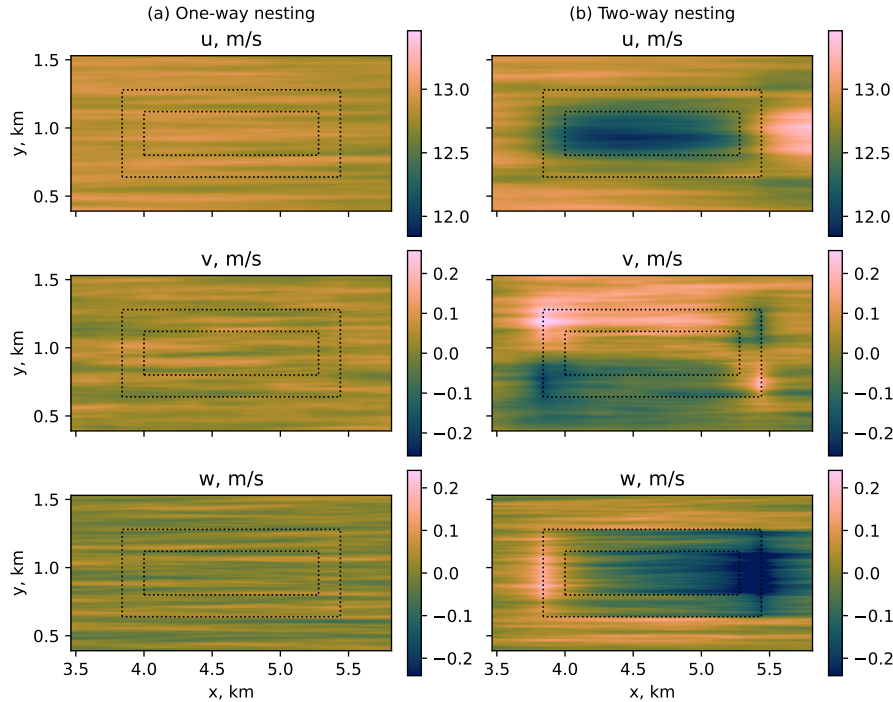
Figure 3. SBL, flow at the hub-height of 119 m for different wind speed components, (a) one-way nesting, (b) two-way nesting.

develops faster, and some of the quantities, particularly, vertical velocity w are not uniformly distributed inside the child domains (Fig. 4).

4.2 Turbulence characteristics

Since the flow is driven by the pressure gradient instead of the Coriolis force, the flow is aligned with x-axis and the wind direction remains nearly constant. The fluctuations of the lateral component v are stronger for the measurement time series. Therefore, we compare turbulence statistics of the horizontal wind speed u from the LES results to the total horizontal flow in the measurements $U = \sqrt{u^2 + v^2}$ and omit the lateral component v for the LES data.

In the one-way nested simulation, the parent domain does not receive feedback from the child domain. Consequently, the spectral characteristics of non-nested domains with the grid spacing of $\Delta_x = 10\,\text{m}$ (NBL and CBL) and $5\,\text{m}$ (SBL) match the characteristics of the corresponding domain in a one-way nesting simulation (Fig. 5, 6). The individual spectra of the nested domains lay apart from each other, but show improvement as the grid spacing is reduced. The inertial subrange resolved by LES widens as the grid becomes more refined; however, it is not fully resolved despite the grid spacing being reduced down to $\Delta_x = 1.25\,\text{m}$.

The two-way nesting mode ensures feedback between the nested domains. Therefore, the root and child domain spectra lie closer to each other and to the one-way spectra of the most refined child domain ($\Delta_x = 1.25\,\text{m}$). Despite the exchange between
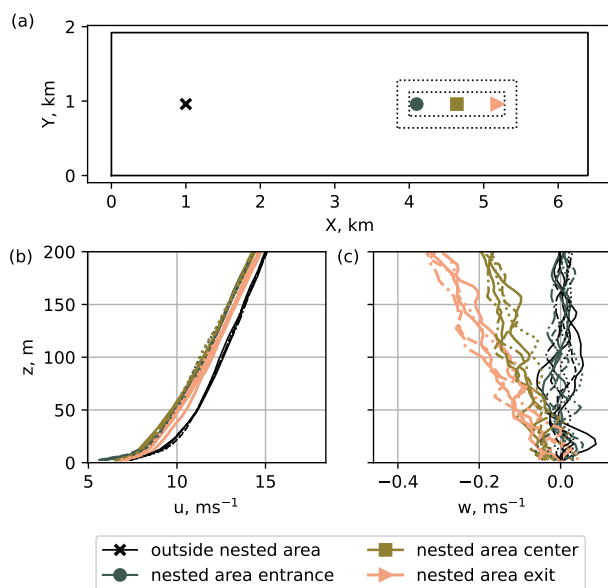
Figure 4. 10-minute average profiles, SBL two-way nested case. (a) Sampling points; (b) the mean flow is slowed down in the nested area; (c) the vertical flow near the entrance of the nested area remains weak, but becomes stronger as the flow passes through the nested area.
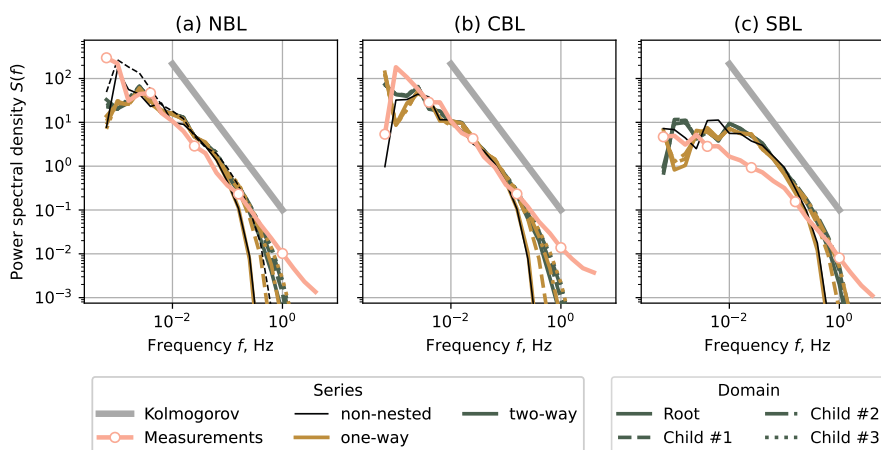
Figure 5. Spectra for the horizontal velocity u at the height $z = 80\,\text{m}$. (a) NBL case, (b) CBL case, (c) SBL case.

185   domains in the two-way nested case, the spectral characteristics do not coincide perfectly. The inertial subrange being shorter for $\Delta_x = 10\,\text{m}$ than for the refined domains implies that the grid resolution is the limiting factor, and the solution for the root domain cannot be improved further even in the two-way nesting case.
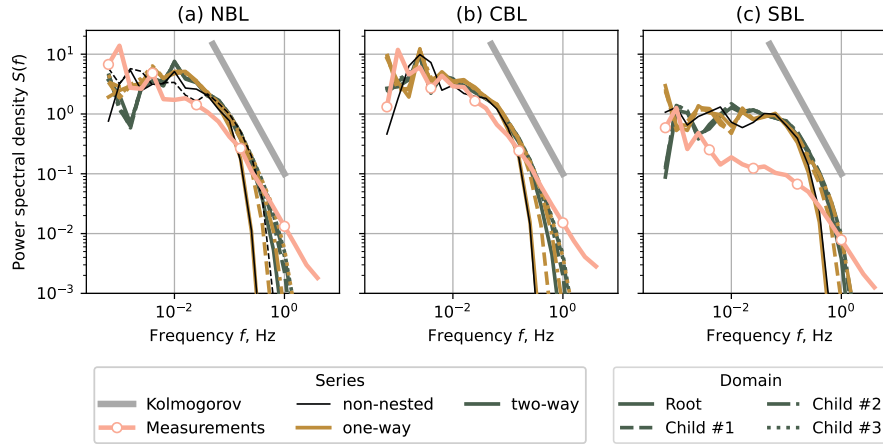
Figure 6. Spectra for the vertical velocity w at the height $z = 80\,\mathrm{m}$. (a) NBL case, (b) CBL case, (c) SBL case.

Despite the NBL case was simulated as the true neutral condition, it showed good agreement with the measurements on par with the CBL case. The result suggests that it is possible to omit the weak heat flux in neutral cases to save computational time and avoid secondary circulation in the two-way nesting mode.

The SBL simulations largely overestimate the energy contained in the low-frequency eddies. Additionally, the inertial sub-range of the corresponding measurement time series starts at higher frequencies, unlike observed in the NBL and CBL cases. High frequencies are not fully resolved by the LES despite the gradual reduction of the grid spacing, hence the overall agreement for the SBL case is worse than for NBL and CBL. We hypothesize that the effect could be caused by the actual boundary layer being substantially lower than simulated and ending below the hub height (119 m). However, we lack the measurement data above 100 m for the particular period to make any conclusions. The existing studies on SBL simulations with PALM model (Beare et al., 2006; Wurps et al., 2020) evaluate other aspects such as fluxes and grid resolution influence, but do not compare simulated spectra against measurements. Hence, simulating SBL in PALM may require additional studies with the focus on turbulence characteristics.

The coherence, co-coherence and phase are plotted against the reduced frequency

$$f_r = \frac{f\delta}{\overline{u}} \tag{8}$$

where f is the original frequency, δ is the vertical separation distance and $\overline{u}$ is the mean wind speed of the two regarded levels: 60 m and 80 m for $\delta = 20\,\mathrm{m}$, or 40 m and 80 m for $\delta = 40\,\mathrm{m}$.

The coherence and co-coherence calculated for NBL and CBL coarse domains ($\Delta_x = 10\,\mathrm{m}$) and $\delta = 20\,\mathrm{m}$ show strong deviation from the measurements for the one-way and non-nested simulations at $f_r > 1$ (Fig. 7a, 8a). The tendency to the coherence/co-coherence value of 0.5 suggests that the time series at points separated by $\delta = 20\,\mathrm{m}$ remain partially correlated in the coarse grid, which is not the case for the corresponding measurements. While the most refined child domain ($\Delta_x = 1.25\,\mathrm{m}$)
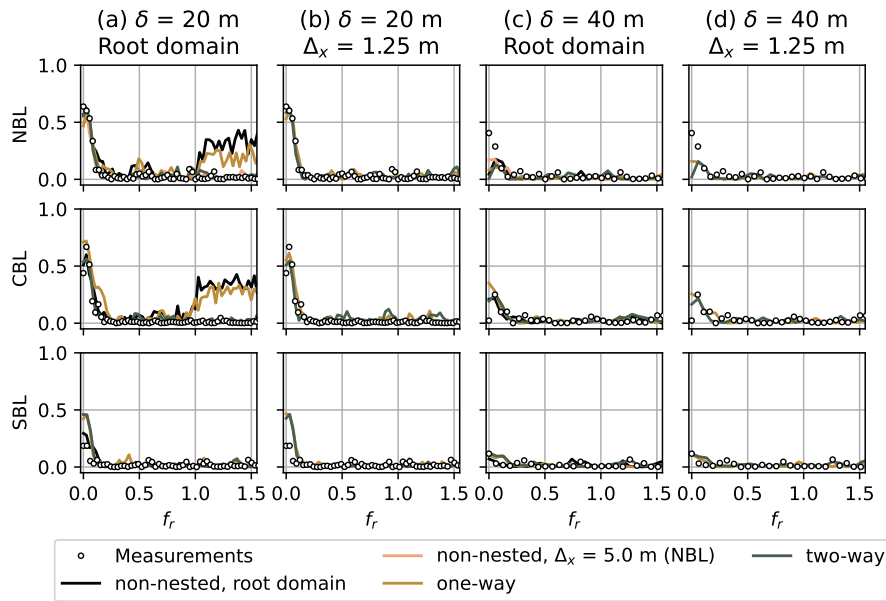
Figure 7. Coherence for the horizontal velocity u and different stability cases. (a) Root domain ($\Delta_x = 10\,\mathrm{m}$ for NBL and CBL, $\Delta_x = 5\,\mathrm{m}$ for SBL), vertical separation $\delta = 20\,\mathrm{m}$. (b) Innermost child domain ($\Delta_x = 1.25\,\mathrm{m}$, all cases), vertical separation $\delta = 20\,\mathrm{m}$. (c) Root domain ($\Delta_x = 10\,\mathrm{m}$ for NBL and CBL, $\Delta_x = 5\,\mathrm{m}$ for SBL), vertical separation $\delta = 40\,\mathrm{m}$. (d) Innermost child domain ($\Delta_x = 1.25\,\mathrm{m}$, all cases), vertical separation $\delta = 40\,\mathrm{m}$.

shows a good match between the LES and measurement series (Fig. 7b, 8b), the agreement already improves for $\Delta_x = 5\,\mathrm{m}$ and the correlation falls to zero for $f_r > 0.5$.

210   The time series are generally uncorrelated for the vertical separation of $\delta = 40\,\mathrm{m}$ both for the LESs and measurements (Fig. 7cd, 8cd). However, the NBL case does not capture high coherence value of $f_r = 0$ observed in the measurements. The SBL case shows better agreement for the root domain because of the lower initial grid spacing $\Delta_x = 5\,\mathrm{m}$. Yet, the coherence is noticeably overestimated for low f_r compared to the measurements.

The phase plots are in line with the coherence. The time series are in-phase for $f_r < 0.1$, where the coherence is above zero.
215   The effect is strong for the low vertical separation of $\delta = 20\,\mathrm{m}$ (Fig. 9ab) and is in good agreement with the measurements. The phase becomes more chaotic as the vertical separation distance increases to $\delta = 40\,\mathrm{m}$ (Fig. 9cd), while the time series become less correlated (Fig. 7cd, 8cd).

4.3   Other flow characteristics

4.3.1   Power law

220   The estimated power law coefficient α shows little variation for the NBL and CBL two-way nested runs, but implies high sensitivity of the SBL profiles (Table 6). In general, the power law coefficient follows the known trend, also observed in the
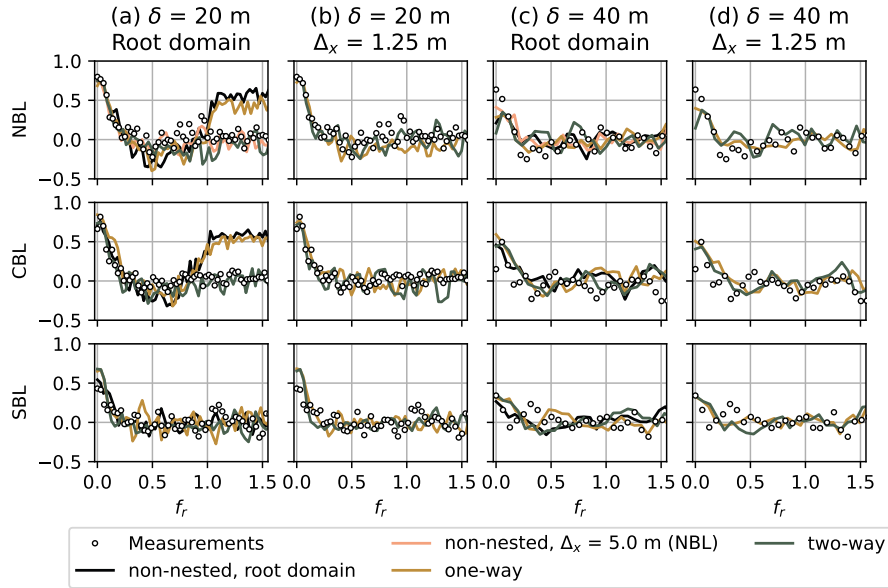
Figure 8. Co-coherence for the horizontal velocity u and different stability cases. (a) Root domain ($\Delta_x = 10\,\text{m}$ for NBL and CBL, $\Delta_x = 5\,\text{m}$ for SBL), vertical separation $\delta = 20\,\text{m}$. (b) Innermost child domain ($\Delta_x = 1.25\,\text{m}$, all cases), vertical separation $\delta = 20\,\text{m}$. (c) Root domain ($\Delta_x = 10\,\text{m}$ for NBL and CBL, $\Delta_x = 5\,\text{m}$ for SBL), vertical separation $\delta = 40\,\text{m}$. (d) Innermost child domain ($\Delta_x = 1.25\,\text{m}$, all cases), vertical separation $\delta = 40\,\text{m}$.

Table 6. Estimated power law coefficient.

| Nesting | Δ_x, m | Power law coefficient α | | |
		NBL	CBL	SBL
non-nested	10	0.111	0.087	-
non-nested	5	0.103	-	0.153
one-way	10	0.112	0.088	-
one-way	5	0.104	0.081	0.144
one-way	2.5	0.095	0.073	0.143
one-way	1.25	0.094	0.070	0.154
two-way	10	0.112	0.088	-
two-way	5	0.099	0.083	0.154
two-way	2.5	0.094	0.081	0.159
two-way	1.25	0.093	0.080	0.166
Measurements		0.061	0.023	0.237
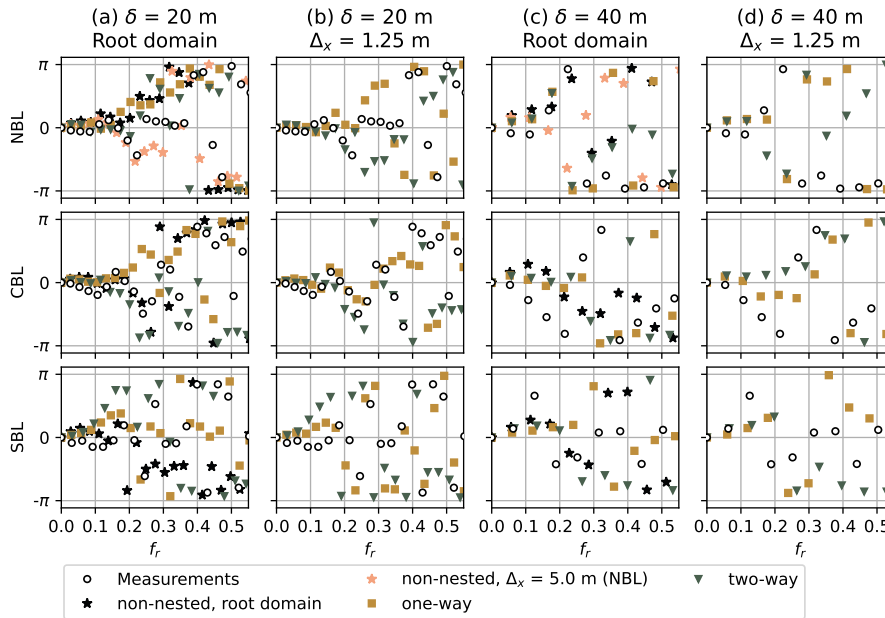
Figure 9. Phase plot for the horizontal velocity u and different stability cases and domains. (a) Root domain ($\Delta_x = 10\,\text{m}$ for NBL and CBL, $\Delta_x = 5\,\text{m}$ for SBL), vertical separation $\delta = 20\,\text{m}$. (b) Innermost child domain ($\Delta_x = 1.25\,\text{m}$, all cases), vertical separation $\delta = 20\,\text{m}$. (c) Root domain ($\Delta_x = 10\,\text{m}$ for NBL and CBL, $\Delta_x = 5\,\text{m}$ for SBL), vertical separation $\delta = 40\,\text{m}$. (d) Innermost child domain ($\Delta_x = 1.25\,\text{m}$, all cases), vertical separation $\delta = 40\,\text{m}$.

measurement profile fits: high value in the stable layer and low value in the convective layer (Touma, 1977). The discrepancy between exact values of α in measurement and simulated fits could be explained by less precise power law fit in the measurement profiles: only three points were available for the fit.

4.3.2 Turbulence anisotropy

The NBL simulation performs best in the two-way nested case for the most refined child domains (Fig. 10). Similar trend of the ratios S_{vv}/S_{uu}, S_{ww}/S_{uu} decreasing with the grid refinement can be seen for other stability cases. However, the values do not approach 1.333 simultaneously and also show a mismatch for the vertical and lateral flow. The turbulence in the PALM-simulated flow becomes more anisotropic when the heat flux is present, although the anisotropy strength may not match the one seen from the measurement data. The divergence is particularly strong for the SBL simulation, which is primarily caused by the differences in power density spectra discussed in Sec. 4.2.

		NBL		CBL		SBL	
		S_{vv}/S_{uu}	S_{ww}/S_{uu}	S_{vv}/S_{uu}	S_{ww}/S_{uu}	S_{vv}/S_{uu}	S_{ww}/S_{uu}
non-nested	10 m	1.431	1.157	1.560	1.570		
non-nested	5 m	1.637	1.437			1.805	1.276
one-way	10 m	1.722	1.576	1.589	1.680		
one-way	5 m	1.449	1.481	1.381	1.391	1.608	1.363
one-way	2.5 m	1.388	1.450	1.270	1.270	1.434	1.274
one-way	1.25 m	1.152	1.281	1.188	1.175	1.396	1.266
two-way	10 m	1.390	1.431	1.576	1.607		
two-way	5 m	1.428	1.393	1.238	1.590	1.330	1.277
two-way	2.5 m	1.382	1.362	1.074	1.386	1.282	1.289
two-way	1.25 m	1.367	1.353	1.003	1.313	1.272	1.293
measurements		1.293	1.152	1.390	1.039	1.027	0.436

Figure 10. Comparison of anisotropy across the regarded stability and nesting cases. The colormap is centered at the value $4/3 = 1.333$.

5 Conclusions

We performed nested LES of three stability cases for the same mean wind speed of $12.5\,\mathrm{ms}^{-1}$ and verified the simulation by comparing the turbulence characteristics to the corresponding measurement time series. The comparison showed that the

235   grid spacing of $\Delta_x = 10\,\mathrm{m}$ was insufficient for NBL and CBL simulations; the spectral and coherence characteristics had improved their agreement with the measurements after the spacing was reduced to $\Delta_x = 5\,\mathrm{m}$ via nesting or a refined non-nested domain simulation. The inertial subrange was not fully resolved despite further refinement and remained narrower than for the measurement time series even at $\Delta_x = 1.25\,\mathrm{m}$.

We confirmed that the nesting mode does not affect the true neutral simulation, unlike the cases when the temperature

240   equation is solved along other prognostic equations for the CBL and SBL conditions. In the case of CBL or SBL, the flow inside the child domain differed for the one-way and two-way nesting. The two-way nested simulation produced a secondary circulation resulting in a decreased velocity and increased turbulence intensity in the child domains. Due to the strong horizontal flow, the irregularities in the lateral and vertical velocity were spread non-uniformly, e.g., the downward flow was stronger at the exit of the nested domain. The horizontal flow accelerated after leaving the nested area so that the mass conservation law

245   was not violated eventually.

In theory, the two-way nesting is a good option to refine the grid in the area of interest of the non-homogeneous flow, e.g., wind turbine wakes, as the feedback between parent and child domain allows simulating the irregularities after the flow exits the nested area. However, the fast development of the secondary circulation in a shear-driven flow limits the two-way nesting application to the neutral conditions. The one-way nested simulation did not add anomalies to the flow; each child domain only

250 improved the grid spacing and resolved small turbulence scales. We, therefore, recommend using either true neutral simulation or one-way nesting for the wind turbine wake simulation.

Code and data availability. The PALM model system is freely available at https://palm.muk.uni-hannover.de (last access: October 12, 2022) and distributed under the GNU General Public License v3 (http://www.gnu.org/copyleft/gpl.html, last access: October 12, 2022). The LESs in this article were performed using PALM model system v21.10. The corresponding version is provided at https://doi.org/10.5281/zenodo.

255 7311217 (Krutova, 2022) together with input and output files, post-processing scripts needed to reproduce the figures. The processed high-frequency sonic anemometer are available upon request after the permission from DEWI (Deutsches Windenergi Institut) is granted.

Author contributions. MK performed the LES simulations and analysis in accordance to the plan developed by MPB; JR and FGN provided valuable discussion on explaining the discrepancies with the measurement data.

Competing interests. The authors declare that they have no conflict of interest.

260 *Acknowledgements.* The authors would like to thank DEWI (Deutsches Windenergi Institut) for providing the FINO1 high-resolution sonic anemometer data and Astrid Nybø from University of Bergen for the additional information and guidance.

The LES simulations for the study have been performed by using the high performance computer facilities of the Norwegian e-infrastructure Uninett Sigma2 (project number NS9696K).

References

Beare, R. J., Macvean, M. K., Holtslag, A. A., Cuxart, J., Esau, I., Golaz, J. C., Jimenez, M. A., Khairoutdinov, M., Kosovic, B., Lewellen, D., Lund, T. S., Lundquist, J. K., McCabe, A., Moene, A. F., Noh, Y., Raasch, S., and Sullivan, P.: An Intercomparison of Large-Eddy Simulations of the Stable Boundary Layer, Boundary-Layer Meteorol. 2006 1182, 118, 247–272, https://doi.org/10.1007/S10546-004-2820-6, 2006.

Bratton, D. C. and Womeldorf, C. A.: The wind shear exponent: Comparing measured against simulated values and analyzing the phenomena that affect the wind shear, in: ASME 2011 5th Int. Conf. Energy Sustain. ES 2011, PARTS A, B, AND C, pp. 2245–2251, American Society of Mechanical Engineers Digital Collection, https://doi.org/10.1115/ES2011-54823, 2011.

Dimitrov, N., Natarajan, A., and Mann, J.: Effects of normal and extreme turbulence spectral parameters on wind turbine loads, Renew. Energy, 101, 1180–1193, https://doi.org/10.1016/j.renene.2016.10.001, 2017.

Golbazi, M. and Archer, C. L.: Methods to estimate surface roughness length for offshore wind energy, Adv. Meteorol., 2019, https://doi.org/10.1155/2019/5695481, 2019.

Haering, S. W., Lee, M., and Moser, R. D.: Resolution-induced anisotropy in large-eddy simulations, Phys. Rev. Fluids, 4, 114 605, https://doi.org/10.1103/PhysRevFluids.4.114605, 2019.

Hellsten, A., Ketelsen, K., Sühring, M., Auvinen, M., Maronga, B., Knigge, C., Barmpas, F., Tsegas, G., Moussiopoulos, N., and Raasch, S.: A nested multi-scale system implemented in the large-eddy simulation model PALM model system 6.0, Geosci. Model Dev., 14, 3185–3214, https://doi.org/10.5194/gmd-14-3185-2021, 2021.

Jung, C. and Schindler, D.: The role of the power law exponent in wind energy assessment: A global analysis, Int. J. Energy Res., 45, 8484–8496, https://doi.org/10.1002/ER.6382, 2021.

Krutova, M.: PALM v21.10 self-nested LES for three stability conditions, https://doi.org/10.5281/zenodo.7311217, 2022.

Maronga, B., Banzhaf, S., Burmeister, C., Esch, T., Forkel, R., Fröhlich, D., Fuka, V., Gehrke, K. F., Geletič, J., Giersch, S., Gronemeier, T., Groß, G., Heldens, W., Hellsten, A., Hoffmann, F., Inagaki, A., Kadasch, E., Kanani-Sühring, F., Ketelsen, K., Khan, B. A., Knigge, C., Knoop, H., Krč, P., Kurppa, M., Maamari, H., Matzarakis, A., Mauder, M., Pallasch, M., Pavlik, D., Pfafferott, J., Resler, J., Rissmann, S., Russo, E., Salim, M., Schrempf, M., Schwenkel, J., Seckmeyer, G., Schubert, S., Sühring, M., von Tils, R., Vollmer, L., Ward, S., Witha, B., Wurps, H., Zeidler, J., and Raasch, S.: Overview of the PALM model system 6.0, Geosci. Model Dev., 13, 1335–1372, https://doi.org/10.5194/gmd-13-1335-2020, 2020.

Moeng, C. H., Dudhia, J., Klemp, J., and Sullivan, P.: Examining two-way grid nesting for large eddy simulation of the PBL using the WRF model, Mon. Weather Rev., 135, 2295–2311, https://doi.org/10.1175/MWR3406.1, 2007.

Munters, W., Meneveau, C., and Meyers, J.: Shifted periodic boundary conditions for simulations of wall-bounded turbulent flows, Phys. Fluids, 28, 025 112, https://doi.org/10.1063/1.4941912, 2016.

Nybø, A., Nielsen, F. G., and Reuder, J.: Processing of sonic anemometer measurements for offshore wind turbine applications, Journal of Physics: Conference Series, 1356, https://doi.org/10.1088/1742-6596/1356/1/012006, 2019.

Nybø, A., Nielsen, F. G., Reuder, J., Churchfield, M. J., and Godvik, M.: Evaluation of different wind fields for the investigation of the dynamic response of offshore wind turbines, Wind Energy, 23, 1810–1830, https://doi.org/10.1002/we.2518, 2020.

Smedman, A.-S., Högström, U., and Sjöblom, A.: A Note on Velocity Spectra in the Marine Boundary Layer, Boundary-Layer Meteorol., 109, 27–48, https://doi.org/10.1023/A:1025428024311, 2003.

300   Stull, R.: An Introduction to Boundary Layer Meteorology, Atmospheric and Oceanographic Sciences Library, Springer Netherlands, https://doi.org/https://doi.org/10.1007/978-94-009-3027-8, 1988.

Touma, J. S.: Dependence of the wind profile power law on stability for various locations, J. Air Pollut. Control Assoc., 27, 863–866, https://doi.org/10.1080/00022470.1977.10470503, 1977.

Witha, B., Steinfeld, G., and Heinemann, D.: High-Resolution Offshore Wake Simulations with the LES Model PALM, Springer, Berlin,
305   Heidelberg, https://doi.org/10.1007/978-3-642-54696-9_26, 2014.

Wurps, H., Steinfeld, G., and Heinz, S.: Grid-Resolution Requirements for Large-Eddy Simulations of the Atmospheric Boundary Layer, Boundary-Layer Meteorol., 175, 179–201, https://doi.org/10.1007/s10546-020-00504-1, 2020.